

Synthesis and characterization of Nickel Metavanadate ($\text{Ni}_3\text{V}_2\text{O}_8$)-application as photocatalyst and supercapacitor

Lakshmana Naik Ramavathu ^{1,*}, Seshagiri Rao Harapanahalli ², Nagaraja Pernapati ²,
BalaNarsaiah Tumma¹

¹Department of Chemical Engineering, JNTUACEA, Ananthapuramu-515002, India

²Department of Chemistry, Rajiv Gandhi University of Knowledge Technologies, RK Valley,
Kadapa-516330, India

Received 15 February 2021, revised 06 May 2021, accepted 12 June 2021, available online 15 June 2021

Abstract

With the emerging newer energy storage applications, transition metal vanadates are booming up as a better catalyst. Among all the transition metal vanadates, nickel vanadate nanoparticles ($\text{Ni}_3\text{V}_2\text{O}_8$ NPs), are considered as a promising material with electrocatalytic and photocatalytic activity. We herein report circular and oval structured $\text{Ni}_3\text{V}_2\text{O}_8$ NPs by hydrothermal route without using any capping agent. Crystallinity, physical structure and morphology of the prepared samples were studied by XRD, TEM, and FT-IR spectroscopy. Photocatalytic activity of $\text{Ni}_3\text{V}_2\text{O}_8$ NPs was studied by decolorizing industrially hazardous dyes such as malachite green (MG) and methylene blue (MB) dyes under ultra-violet light conditions for a regular interval of time (15 min) to 90 min. The experiment shows decolorization efficiencies as 52.43 and 57.66% for MG and MB, respectively. The electrochemical behaviour of the prepared compound was studied, and Energy storage capacity (specific capacitance) was elucidated as 193.5 Fg^{-1} with high reversibility property the material. These results indicated that $\text{Ni}_3\text{V}_2\text{O}_8$ is a promising electrode material for supercapacitor and is an excellent photocatalyst. Hence, hydrothermally synthesized $\text{Ni}_3\text{V}_2\text{O}_8$ NPs are expected to offer significant insight into their multifunctional applications.

Keywords: Dye Degradation; Malachite Green (MG); Methylene Blue (MB); Nickel Vanadate; Photocatalysis; Supercapacitor.

How to cite this article

Naik Ramavathu L, Rao Harapanahalli S, Pernapati N, Tumma B. Synthesis and characterization of Nickel Metavanadate ($\text{Ni}_3\text{V}_2\text{O}_8$)-application as photocatalyst and supercapacitor. *Int. J. Nano Dimens.*, 2021; 12(4): 411-421.

INTRODUCTION

In recent years, due to the enormous growth in the world population, energy has become a basic need for everyone and plays a crucial role in the country's economic, industrial, and overall development. The necessity of the energy cannot be decreased by time. Present society energy has depended on fossil fuels, energy storage becomes challenging and not economical, which attracts scientists to work on efficient energy utilization [1, 2]. There are various ways in which energy can be stored [3, 5]. Among which supercapacitors are the new avenue in energy storage and lied forefront of the environmentally healthy electrochemical energy storage systems compared to traditional

batteries, which are linked to pollution [6, 9]. Based on working mechanisms, supercapacitors are broadly grouped into two classes: electric double-layer capacitors (EDLCs) and pseudo capacitors. EDLCs electrode material mainly contains carbon (C) content, whereas pseudo capacitor electrode includes metal oxides and metal hydroxide conducting polymers [10, 11]. Most common material is Ruthenium oxide due to its capacitance properties through fast reversible multielectron surface faradic redox reactions. Eventually, there has been mounting attention in transition metal oxides due to their augmented combination, various morphological features and crystallinity related electrode resources for energy storage and generation devices [12, 14].

* Corresponding Author Email: lakshman2027@gmail.com

It has led to rising curiosity in ornamental the electrochemical effectiveness and purification of water by nanostructures of metal oxide to be used as a catalyst for both anode and cathode. For many areas of human life, their unique size-dependent characteristics make these materials essential and outstanding. Nickel is the most common transition metal in the Earth's crust and is the cornerstone of modern infrastructure. In recent years, in light of their essential and technological aspects, metal oxides have become the focus of the investigation [15, 16]. Nickel-based vanadium oxide is an excellent catalyst between different metal oxides, and so many fundamental researches on catalytic oxidation have all been reported [17, 18]. Among these, vanadium generates several oxygen compounds; they have various optical, structural, and chemical properties. The major properties variations between various phases of vanadium oxides relay on their arrangement that defines certain characteristics. A significant number of vanadium oxide nanostructures, including nanorods, nanobelts and nanowires, were examined for their usage as electrode materials [19]. Vanadium nanotubes offer an ability to use metal cation Vanadium oxide to increase the electrochemical productivity of a nanostructure.

At the current time, advanced specific capacitance values were shown by binary metal oxides pseudo capacitors due to the fact that binary metal oxides multiple oxide states, excellent electrical conduction and outstanding electrochemical behaviour described previous $Zn_3V_2O_8$, $CoMoO_4$ and $ZnFe_2O_4$. Vanadium oxide (VO_x) based electrode materials as both cathode and anode for Li-ion batteries got attention in the field due to their good crystallinity and varied morphologies. Different electrochemical behaviours have been displayed by the vanadium oxide due to its multivalent nature [20, 21].

Present work reports the preparation of $Ni_3V_2O_8$ nanostructures by simple hydrothermal route. The photocatalytic activity (PCA) of the nanostructures was performed on MG and MB dyes under UV light irradiation at a regular interval of time. The prepared $Ni_3V_2O_8$ were characterised for crystallinity, phase, structural and morphological properties. Detailed study of the super capacitive property of the electrode material has been performed in 0.1M HCl using CV and EIS techniques. This work depicts the intention to utilize mixed ferrites based photocatalytic and

electrochemical studies for a broad spectrum of energy and water treatment applications to promote sustainable, eco-friendly and cleaner technologies for the better tomorrow.

EXPERIMENT

Materials

Materials used for the preparation of $Ni_3V_2O_8$ were of analytical reagent (AR) grade purchased from Sigma Aldrich, Germany they are Nickel (II) nitrate hexahydrate ($Ni(NO_3)_2 \cdot 6H_2O$), Ammonium metavanadate (NH_4VO_3 , $\geq 99.0\%$), N-methyl-2-pyrrolidone (C_5H_9NO), urea (CH_4N_2O), Graphene oxide (GO), ethanol (C_2H_5OH) and double distilled water (H_2O , lab made). Malachite green (MG) and methylene blue (MB) dye powders for photocatalytic activity.

Preparation of catalyst

Modified Hummers method was incorporated in order to synthesis Graphene Oxide (GO) powder. Preparation of Nickel vanadate ($Ni_3V_2O_8$) catalyst was via simple hydrothermal technique. In brief, firstly, 1.323 grams of NH_4VO_3 white powder was added in to 87.5 mL of N-Methyl-2-Pyrrolidone while constant uniform magnetic stirring about 1 hour. 8.45 grams of urea was added to the above solution, and the stirring was continued. Aqueous Nickel nitrate solution was prepared by dissolving 5.036 grams of $Ni(NO_3)_2 \cdot 6H_2O$ in 240mL of double distilled water and added slowly to the above solution with continuous and constant stirring. To this mixture, 8mg of GO (prepared by modified Hummers method) stored in DMF was added. All the contents were transferred into a Teflon lined autoclave (500ml capacity), and the volume was adjusted to 350ml with distilled water. Sealed autoclaves were maintained at 180 °C for 10 hours in a muffle furnace for thermal digestion under elevated pressures. After conventional furnace cooling to room temperature, the final product was collected by centrifugation, a thorough wash with double distilled water, ethanol and dried at 80 °C. The dried samples were calcinated at 450 °C for 3 hours with a heating rate of 2 °C per min^{-1} to get highly crystalline nanostructures. The calcined sample was taken for further characterization.

Characterization

A Schimadzu x-ray diffractometer (PXRD-7000) with $CuK\alpha$ radiation ($\lambda=1.541 \text{ \AA}$) was used to study the crystalline features of the sample

in the 2θ range from $20\text{--}80^\circ$. Fourier transform-infrared (FTIR) spectroscopy was performed using a Perkin Elmer FTIR Spectrophotometer (Spectrum-1000) with KBr pellets. Uv-Visible (UV-vis) studies were conducted using an Elico SL-150 spectrophotometer in the range from $200\text{--}800\text{ nm}$ using barium sulphate (BaSO_4) as a reference material. The cyclic voltammetry (CV) and electrochemical impedance spectroscopy (EIS) measurements were carried out using an electrochemical analyser (CHI608E potentiostat) in a tri-electrode system, comprising a carbon paste electrode (working), platinum wire (counter) and Ag/AgCl (reference electrode) in 0.1M HCl as the electrolyte. Electrochemical impedance spectroscopy measurements in the frequency range from 1Hz to 1MHz were performed at 5mV AC amplitude [22].

RESULTS AND DISCUSSION

Fig. 1. Shows XRD patterns of hydrothermally synthesized crystalline $\text{Ni}_3\text{V}_2\text{O}_8$ nanostructures, which assigns clearly all the planes (131), (221), (151), (244) as mentioned in JCPDS card no. 70-1394 space group-Cmca without any impurity with $a=5.931\text{ \AA}$, $b=11.374\text{ \AA}$, $c=8.235\text{ \AA}$, Density: $\rho = 4.85\text{ Mg}\cdot\text{m}^{-3}$. Orthorhombic (space group-Cmca) lattices result from stretching a cubic lattice along 2 of its orthogonal pairs by 2 different factors a/b (0.52) and b/c or $c/a = 1.38$ resulting in a rectangular prism with different lattice parameters (a , b and c) as shown in Table 1 [23]. Using Scherrer's relation the average crystallite size was found and it is 9.03nm for the place (511) peak at $2\theta=44^\circ$.

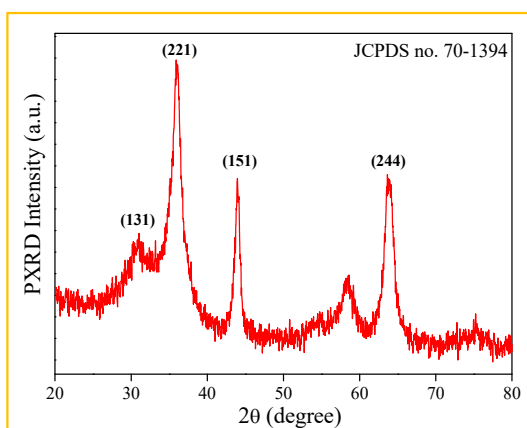


Fig. 1. XRD patterns of $\text{Ni}_3\text{V}_2\text{O}_8$.

$$D = \frac{k\lambda}{\beta \cos\theta} \quad (1)$$

Where, k – diffraction constant (0.9), λ – X-ray wavelength used ($1.54 \times 10^{-10}\text{ m}$), D - crystallite size, β - full-width half-maximum (FWHM), θ - diffraction angle on X-ray incidence. [24].

FTIR spectra were acquired for the prepared $\text{Ni}_3\text{V}_2\text{O}_8$ nanostructures. The peaks observed between the range $500\text{ to }1000\text{cm}^{-1}$ are attributed to V-O and V=O stretching and bending bonds, respectively. The significant patterns in Fig. 2 are in the range of $1460\text{--}1650\text{ cm}^{-1}$ and $2850\text{--}2930\text{ cm}^{-1}$, representing C-H bending and stretching vibrations, respectively. [25]

Fig. 3 depicts energy gap spectra, and the onset figure shows diffusion reflection spectra of $\text{Ni}_3\text{V}_2\text{O}_8$ nanostructures. Kubelka–Munk (SKM) equation (Eqn. 2&3) was used to calculate the energy band gap value and was found to be 2.49eV .

$$F(R) = \frac{(1-R)^2}{2R} \quad (2)$$

$$F(R)hv = A(hv - Eg)^n \quad (3)$$

Where $F(R)$ is the function absolute reflection (R) also called as Kubelka–Munk function, A and hv are constant and an energy of the photon for $n=2$, direct allowed transition and $n = \frac{1}{2}$, indirectly allowed transition. [26, 27]

Fig. 4(a) and 4(b) are Transmission electron

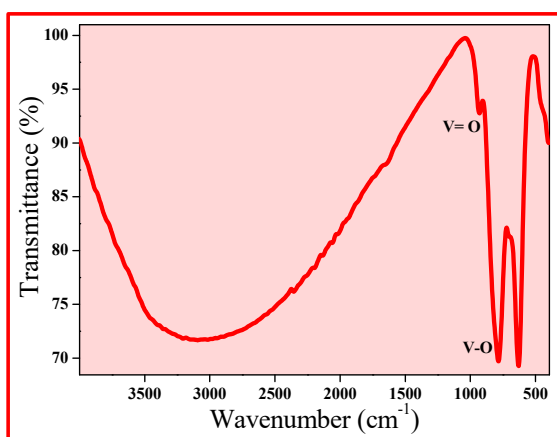


Fig. 2. FTIR spectra of $\text{Ni}_3\text{V}_2\text{O}_8$ to observe the V-O and V=O functional bonds.

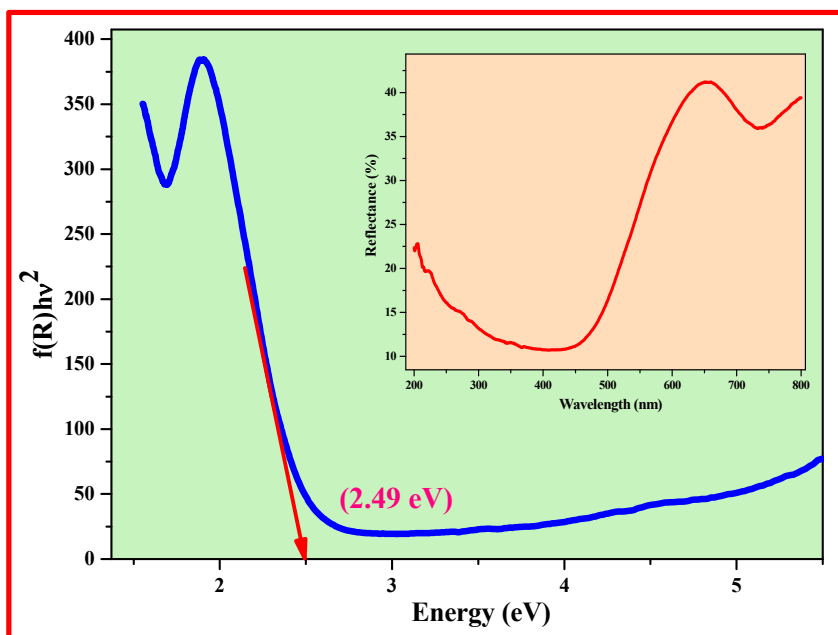


Fig. 3. DRS spectra and Kubelka-Munk function Vs Energy gap of $\text{Ni}_3\text{V}_2\text{O}_8$ showing $E_g=2.49\text{eV}$.

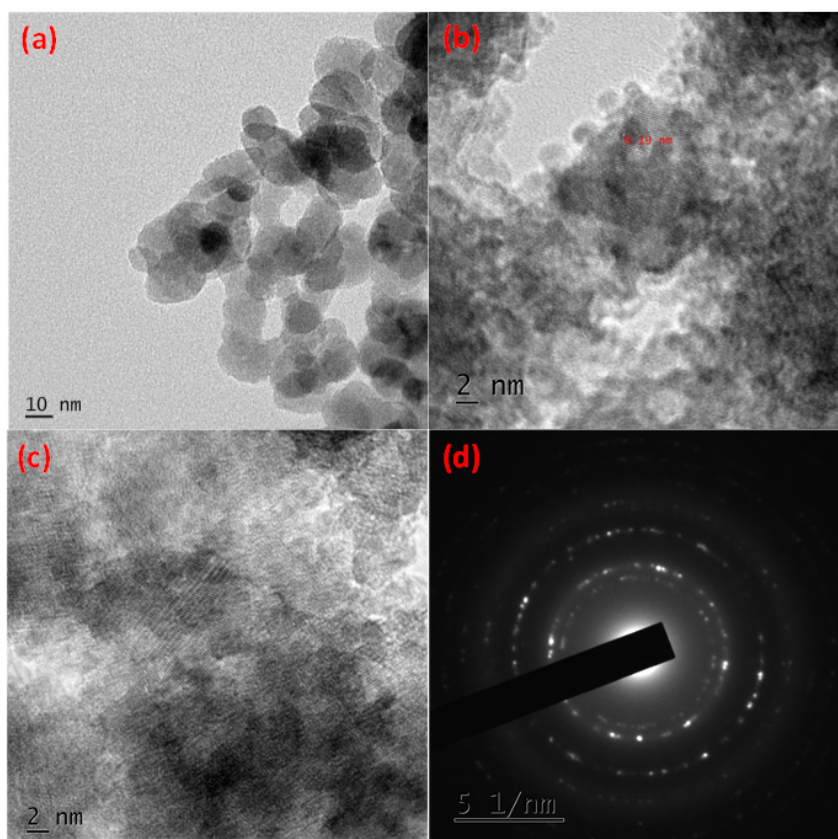
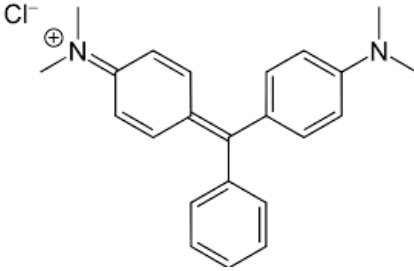
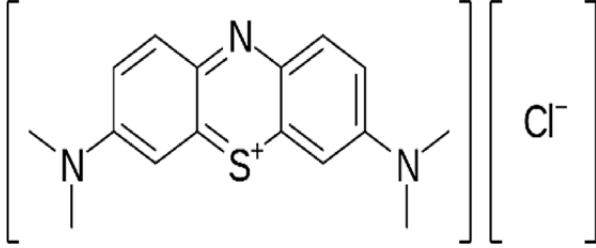


Fig. 4. TEM images (a) micrographs at range 10 nm (b) at range 2 nm (c) High resolution (HR)-TEM picture showing different planes and (d) Selected area emission diffraction (SAED) pattern of $\text{Ni}_3\text{V}_2\text{O}_8$ material.

Table 1. Lattice parameters of Ni₃V₂O₈ Nano structure.

Lattice parameters								
a (\AA)	b (\AA)	c (\AA)	$\alpha=\beta=\gamma$	a/b	b/c	c/a	V (\AA^3)	D (nm) For plane (151)
5.931	11.374	8.235	90°	0.52	1.38	1.38	555.52	9.03
Space group: Cmca								
Structure: orthorhombic								

Table 2. PCA used Dye information with structure and chemical formula.

Name of Dye	Molecular formula	Structure
Malachite green (MG)	C ₂₃ H ₂₅ N ₂	
Methylene blue (MB)	C ₁₆ H ₁₈ ClN ₃ S	

microscopic pictures shows circular and ovular structures of the material and the size slightly varies in the range between 10 nm to 20 nm. Fig. 4(c) shows different crystal planes justifying the formation of the crystalline structure. Fig. 4(d) shows the Selected Area Emission Diffraction (SAED) pattern which confirms the polycrystallinity of the material; all the bright rings correspond to different planes in the prepared Ni₃V₂O₈ material.

Photocatalytic studies:

Both the hazardous and non-eco-friendly carcinogenic dyes (Malachite green (MG) and Methylene blue/methylthionine chloride (MB)) were commonly used in bio and textile industries as given in Table 2. Previous studies on the adverse effects on the human body and environment, such as cyanide poisoning, urinary bladder, and tract infections, made them highly not recommend commercial usage. MB pollution's most general

associated side effects consist of mild and severe headaches, vomiting, nausea, breathing difficulties, and blood pressure (BP), leading to artery disturbance causing heart problems. Some more negative side effects contain syndrome like serotonin, RBC (red blood cell) breakdown and allergies both skin and thought. Often usage of such contaminations leads to saviour indications showing major difficulties in the human body misbehaviour such as change in stool, sweat and urine from blue to green colour. Pregnant may suffer a lot during the delivery and baby conditions if they consume these pollutants in any means [28].

Similarly, the other dye, malachite green (MG), taken as another organic dye, is among the commonly used hazardous candidates in the industries such as silk, leather and paper industry and controversially in the field antimicrobial in aquaculture. Due to its intense colour, solid

samples appear almost greenish-black.

The industrial dyes namely Malachite green (MG) and Methylene blue (MB) degradation studies of simple hydrothermal synthesized $\text{Ni}_3\text{V}_2\text{O}_8$ photocatalyst were studied under the irradiation of ultraviolet light at regular intervals of time (15 min) up to 90 min. MG and MB were selected as representative industrial dyes to evaluate the photo degradation, MG and MB shows absorption peak at 592 and 660nm respectively. First degradation performance was seen in dark condition by considering 20ppm dye solutions separately. It was noted that the dye solution did not undergo noticeable change. Next, degradation studies were conducted under the UV light for some time as an initial confirmation test, and it was observed that noticeable degradation of dye solution. At last, dye degradations studies were performed by considering time as a parameter under UV light irradiation by taking $\text{Ni}_3\text{V}_2\text{O}_8$ as a catalyst for the two dyes separately under room temperature.

Fig. 5(a) and 6(a) depicts the UV absorbance spectrum of MG and MB dye solutions from initial 0min to final 90 min. Percentage degradation plots are given in the respective inset figures. For MG dye the %D values are 0, 15.90, 19.00, 27.57,

31.92, 36.37 and 52.43% for 0, 15, 30, 45, 60, 75 and 90 min respectively and the plot of $\ln(C/\text{Co})$ Vs time (Fig. 5(b)) portrays the same. For MB dye the %D values are 0, 10.01, 23.56, 38.62, 51.31, 53.54 and 57.66 % for 0, 15, 30, 45, 60, 75 and 90 min respectively and the plot of $\ln(C/\text{Co})$ Vs time (Fig. 6(b)) portrays the same. Fig. 5(c) and Fig. 6(c) show dye degradation half-life in which 50% in the time span of 88 min and 58.47 min for MG and MB, respectively. Fig. 5(d) and 6(d) shows percentage removal of total organic carbon (%TOC) which is found at the last trail i.e., 90 min are 49% and 55% for MG and MB dye solution.

Fig. 7. Shows the mechanism of photocatalytic activity under UV irradiation for the proposed dye and catalyst $\text{Ni}_3\text{V}_2\text{O}_8$. When UV light incidents on the $\text{Ni}_3\text{V}_2\text{O}_8$ electrons absorbs UV energy and excites from the valence band (VB) to the conduction band (CB) creating same number of charge carriers namely electrons and holes. The electrons generated in the CB are transferred to the $\text{Ni}_3\text{V}_2\text{O}_8$ catalyst and initiate reaction with the atmospheric O_2 to form superoxide radicals. Meanwhile, the holes in the VB will react with the H_2O and grows hydroxyl radicals. The superoxide radicals that were produced during dye activation phenomena will boost the degradation of the dye

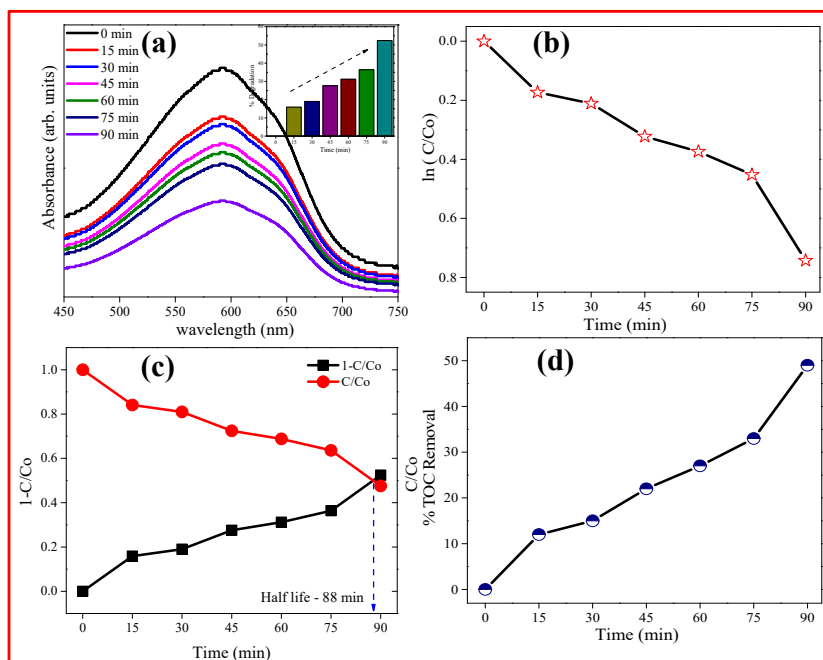


Fig. 5. (a) Absorbance spectra of MG (20 ppm) dye solution with $\text{Ni}_3\text{V}_2\text{O}_8$ catalyst, inset: % degradation of MG dye solution under UV irradiation. (b) $\ln(C/\text{Co})$ Vs time plot (c) Half-life plot - $\ln(C/\text{Co})$ Vs time plot (c) Plot of $1-C/\text{Co}$ and C/Co Vs time under UV irradiation. (d) % TOC removal plot.

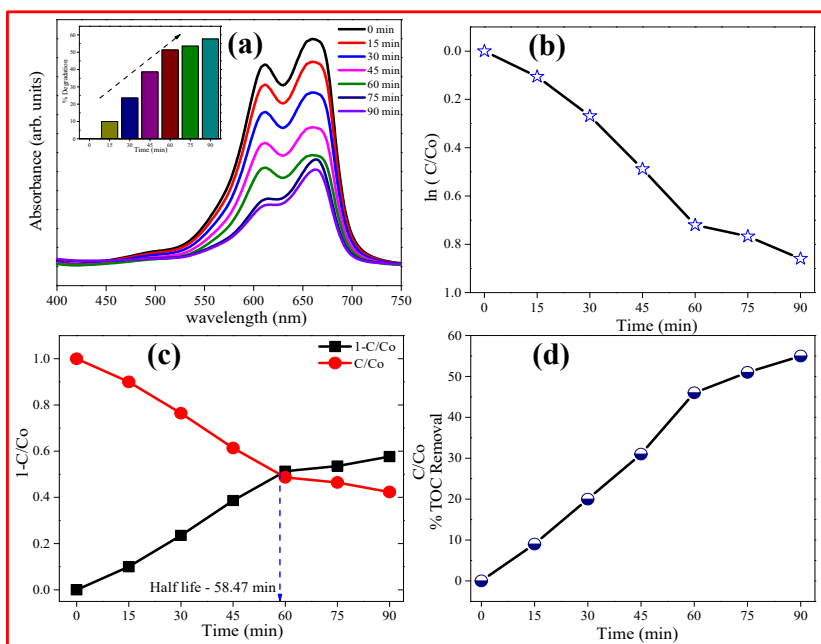


Fig. 6. (a) Absorbance spectra of MB (20 ppm) dye solution with $Ni_3V_2O_8$ catalyst, inset: % degradation of MB dye solution under UV irradiation. (b) Half-life plot - $\ln(C/C_0)$ Vs time plot, plot of $1-C/C_0$ and C/C_0 Vs time under UV irradiation. (d) % TOC removal plot.

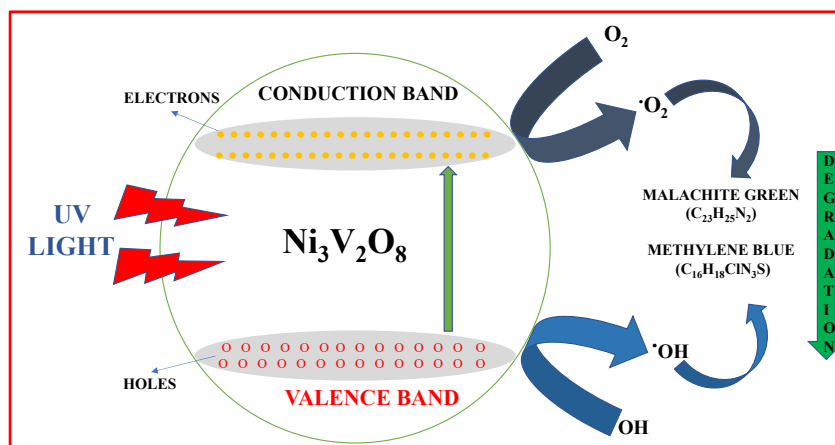
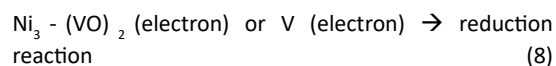
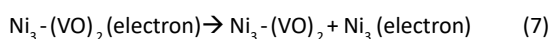
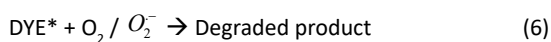
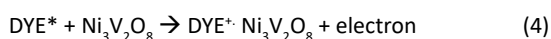


Fig. 7. Mechanism of photocatalytic activity.

molecule. These radicals produced will react with the dye and lastly, break the molecules of the dyes and undergo discoloration (eqn 4-8).



Electrochemical impedance spectroscopic (ESI) studies were done employing cyclic voltammetry (CV) and AC impedance using a 3-electrode cell in 0.1 M (molar) HCl (hydrochloric acid) at room temperature (RT). The Cyclic Voltammogram graphs show the efficiency of charge and electrode reaction reversibility. $Ni_3V_2O_8$ active carbon paste electrode shows (Fig. 8) CV plots

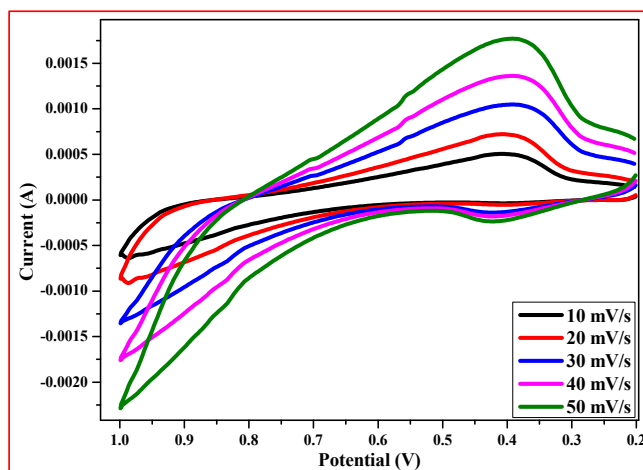


Fig. 8. Cyclic voltammogram of Ni₃V₂O₈.

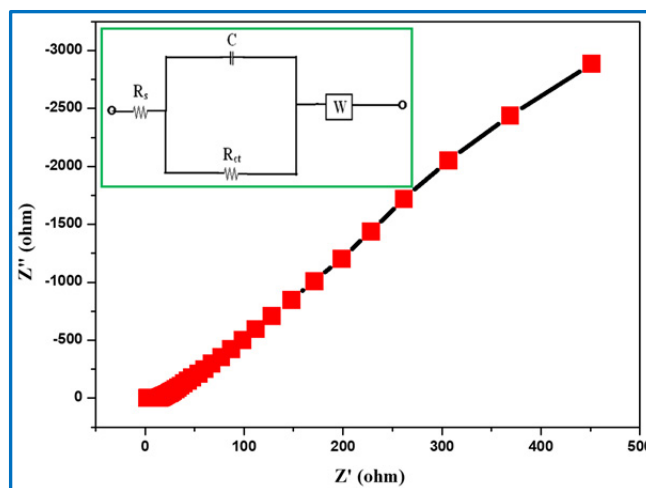


Fig. 9. Nyquist plot with equivalent circuit (Inset) of Ni₃V₂O₈ electrode versus Ag/AgCl in 0.1M HCl.

at a scan rate that varies from 0.010 to 0.050 V/s in 0.1M HCl, respectively. There is a variation in the CV properties due to the scan rates which can be clearly observed in the plots. As the scan rate increases, there is a noticeable increase in the peak current (ip) responsible for both oxidation and reduction, which says there is a quick movement of the electrons in the working electrode interface and mainly at the electrolyte. The CV shows pair of reversible redox maxima as an influence of faradaic reactions of the material (electrode) with ions of the electrolyte (Fig. 9) [29]. The CV results of the electrode are demonstrated a pseudo capacitive property, in determining the capacitance of an electrode ionic conductivity of

the electrolyte plays a major role and these ions have ionic size equal or less than pore size of the used working electrode in order to get the high-power density and large values of capacitance. [30-34]. Due to this hydrated ions dimensions gets majorly affected in ionic conductivity along with the specific capacitance of the electrode. Later this was calculated using a relation (9) [35].

$$C_{sp} = \frac{S}{mk\Delta V} \tag{9}$$

In the above relation S, m, k and ΔV indicates area under the CV curve, weight of the active material used in the electrode, voltage window or the change in the voltage and rate of scanning,

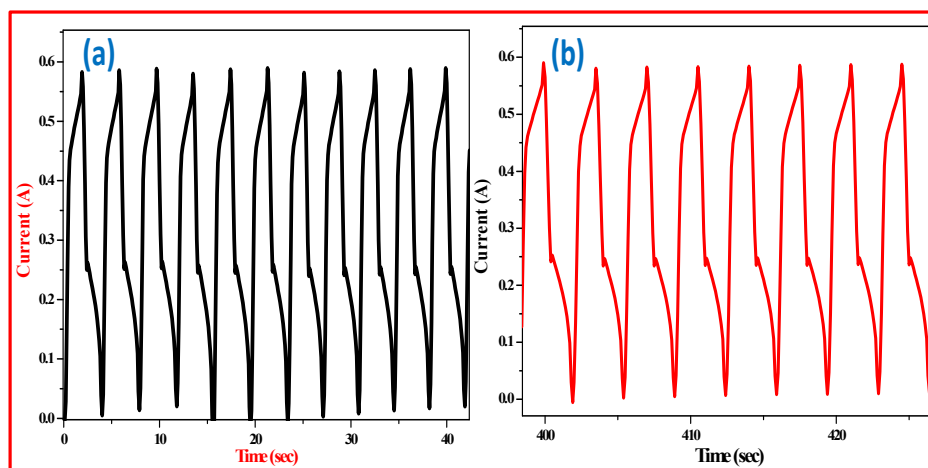


Fig. 10. Galvanostatic charge–discharge curves of $\text{Ni}_3\text{V}_2\text{O}_8$ electrode: (a) 1st ten cycles and (b) last ten cycles of 100 cycles.

respectively. Specific capacitance is directly related to the area under the CV curve for any electrode, which gives overall charge (Q) stored. From this it can be said that large area in the electrode is directly proportional to the production of large capacitance at the known mass of electrode material loaded and potential window. Using Eq. (1), the specific capacitance value for the electrode were calculated as 193.5 Fg^{-1} in 0.1 M HCl.

The charge-transfer (CT) properties of the $\text{Ni}_3\text{V}_2\text{O}_8$ electrode were studied by conducting EI spectra in the electrolyte (0.1 N HCl) in the frequency range between 1 Hz to 1 MHz at 5 mV amplitude (Fig. 8). The intermediate (interface) of the prepared carbon paste active working electrode and electrolyte was determined from the semicircles of Nyquist plots. The EI spectrum of an electrode showed a lowered arc with a smaller radius in the higher frequency range, revealing the low charge transfer resistance (Rct) and high capacitance (C) of the prepared active electrode [36–40]. The above observations are further justified and supported via values of CT resistance (Rct) and capacitance (C) obtained from the equivalent circuit fitting for Nyquist plots (Fig. 8 and Table 1).

Figs. 10 (a, b) show the GCD profile of $\text{Ni}_3\text{V}_2\text{O}_8$ NPs at 5 A/g current density in 0.1M HCl solution. The GCD profile illustrates symmetric charging and discharging curves. Owing to the resistance factor between the interface of electrode and electrolyte, a small IR drop at the point of conversion from charging to discharging can be noticed [41]. The pseudo capacitance nature of the electrode is

responsible for the coulomb efficiency and high reversibility of faradic ion kinetics, which is clear from the symmetric GCD profile of the charging and discharging studies. The specific capacitance $\text{Ni}_3\text{V}_2\text{O}_8$ NPs from the GCD curves can be estimated using the following expression [42]:

$$C_s = \frac{i \Delta t}{m \Delta v} \quad (10)$$

Where, i , m , Δt and Δv are the applied current, mass of the active material loaded onto the substrate, Δt the discharging time and potential (voltage) window. The GCD curve of $\text{Ni}_3\text{V}_2\text{O}_8$ NPs shows appreciable coulomb efficiency after many periodic cycles with retention in a pattern of the curves even after 100 cycles (Fig. 10b).

CONCLUSIONS

$\text{Ni}_3\text{V}_2\text{O}_8$ nano structures were prepared via cost-effective simple hydrothermal method followed by studies on comprehensive structural properties. Studies were extended for the photocatalytic and electrochemical properties. It was concluded that the prepared nanostructures exhibiting the enhanced photocatalytic activity in the degradation of MB and MG under irradiation of UV light. The cyclic voltammograms revealed that the prepared carbon paste electrode content showed uppermost specific capacitance 193.5 Fg^{-1} in 0.1 M HCl at 10 mV/s scan rate. From these evidences, we can say this nanostructure shows better electrochemical activity and photocatalytic activity for applications in Supercapacitor, energy storage devices and in the removal of organic dyes

from the wastewater/water treatment.

ACKNOWLEDGEMENT

The authors would like to thank the Department of Chemical Engineering, MME, and Department of Chemistry RK Valley for the laboratory and FTIR characterization. The author is very grateful to the DST-PURSE Centre of Sri Venkateswara University Tirupati for the physical characterization, and “DST-SAIF Cochin” for the TEM analysis.

CONFLICT OF INTERESTS

There is no conflict of interest.

REFERENCES

- [1] Mahmoudzadeh Andwari A., Pesiridis A., Rajoo S., Martinez Botas R., Esfahanian V., (2017), A review of battery electric vehicle technology and readiness levels. *Renew. Sustain. Energy Rev.* 78: 414–430.
- [2] Balali Y., Stegen S., (2021), Review of energy storage systems for vehicles based on technology, environmental impacts, and costs. *Renew. Sustain. Energy Rev.* 135: 110185-110189.
- [3] Yufei Z., Laiquan L., Haiquan S., Wei H., Xiaochen D., (2015), Binary metal oxide: Advanced energy storage materials in supercapacitors. *J. Mater. Chem. A.* 3: 43-59.
- [4] Guoping W., Lei Zh., JiuJun Zh., (2012), A review of electrode materials for electrochemical supercapacitors. *Chem. Soc. Rev.* 41: 797-828.
- [5] Forouzandeh P., Kumaravel V., Pillai S. C., (2020), Electrode materials for supercapacitors: A Review of recent advances. *Catalysts.* 10: 969-973.
- [6] Venkateswarlu P., Umeshbabu E., Kumar U. N., Nagaraja P., Tirupathi P., (2017), Facile hydrothermal synthesis of urchin-like cobalt manganese spinel for high-performance supercapacitor applications. *J. Colloid Interf. Sci.* 503: 17-27.
- [7] Rajavel V., Ramu M., Justin Raj C., Marotrao Kale A., Kaya C., Palanisamy K., Chul Kim B., (2021), Electrodeposition of vanadium pentoxide on carbon fiber cloth as a binder-free electrode for high-performance asymmetric supercapacitor. *J. Alloys Comp.* 863: 158332-158336.
- [8] Simon Justin A., Vickraman P., Joji Reddy B., (2019), Investigation on Carbonsphere@Nickel Cobalt Sulfide core-shell nanocomposite for asymmetric supercapacitor application. *Energy Harvest. Sys.* 6: 1-13.
- [9] Rajeshkhanna G., Umeshbabu E., Justin P., Rao G. R., (2015), In situ fabrication of porous festuca scoparia-like $Ni_{0.3}Co_{2.7}O_4$ nanostructures on Ni-foam: An efficient electrode material for supercapacitor applications. *Int. J. Hydrog. Energ.* 40:12303-12314.
- [10] Dai Y., Li Q., Tan S., Wei Q., Pan Y., Tian X., Zhao K., Xu X., An Q., Mai L., Zhang Q., (2017), Nanoribbons and nanoscrolls intertwined three-dimensional vanadium oxide hydrogels for high-rate lithium storage at high mass loading level. *Nano Energy.* 40: 73–81.
- [11] Behara D., Priya Alugoti D., Sree P., (2020), Multi element doped type-II heterostructure assemblies (N, S- TiO_2/ZnO) for electrochemical crystal violet dye degradation. *Int. J. Nano Dimens.* 11: 303-311.
- [12] Rajeshkhanna G., Umeshbabu E., Justin P., Rao G. R., (2017), Spinel $ZnCo_2O_4$ nanosheets as carbon and binder free electrode material for energy storage and electroreduction of H_2O_2 . *J. Alloys Comp.* 696: 947-955.
- [13] Arumugam S., Perumal S., Muthusamy G., Murugesan S., Ganesan K., (2020), Tetrabutylammonium perchlorate electrolyte on electrochemical properties of spinel $MgCo_2O_4$ nanoparticles. *Int. J. Nano Dimens.* 11: 26-31.
- [14] Lakshmana Naik R., Justin P., Bala Narsaiah T., (2020), Size controlled hydrothermal synthesis and characterization of nickel metavanadate ($NiVO_3$) nanoparticles. *Int. J. Adv. Sci. Technol.* 29: 10012 – 10018.
- [15] Wenbin F., Xiulei L., Changhui Z., Ying L., Peng Z., Jinyuan Z., Xiaojun P., Erqing X., (2015), Facile hydrothermal synthesis of flowerlike $ZnCo_2O_4$ microspheres as binder-free electrodes for supercapacitors. *Mater. Lett.* 149: 1–4.
- [16] Zamani A., Seyed Sadjadi M., Mahjoub A., Yousefi M., Farhadyar N., (2020), Synthesis and characterization $ZnFe_2O_4@MnO$ and $MnFe_2O_4@ZnO$ magnetic nanocomposites: Investigation of photocatalytic activity for the degradation of Congo red under visible light irradiation. *Int. J. Nano Dimens.* 11: 58-73.
- [17] Khatri B., Rajbhandari A., (2020), Preparation, characterization and photocatalytic application of novel bismuth vanadate/ hydroxyapatite composite. *Adv. J. Chem. Sect. A.* 3: 789-799.
- [18] Sajjadnejad M., Karimi Abadeh H., (2020), Processing of nanostructured TiO_2 and modification of Its photocatalytic behavior for methylene blue degradation. *Adv. J. Chem. Sect. A.* 3: 422-431.
- [19] David Mc., Gillian C., Colm O. D., (2018), $NiVO_3$ fused oxide nanoparticles: An electrochemically stable intercalation anode material for lithium-ion batteries. *J. Mater. Chem. A.* 6: 18103-18107.
- [20] McNulty D., Buckley D., O'Dwyer C., (2014), Polycrystalline vanadium oxide nanorods: Growth, structure and improved electrochemical response as a Li-ion battery cathode material. *J. Electrochem. Soc.* 161: A1321-A1329.
- [21] McNulty D., Buckley D. N., Dwyer C. O., (2016), Comparative electrochemical charge storage properties of bulk and nanoscale vanadium oxide electrodes. *J. Solid State Electrochem.* 20: 1445–1458.
- [22] Ravikumar C. R., Kotteeswaran P., Bheema raju V., Murugan A., Santosh M. S., Nagaswarupa H. P., Prashantha S. C., Anil kumar M. R., Shivakumar M. S., (2017), Influence of zinc additive and pH on the electrochemical activities of β -nickel hydroxide materials and its applications in secondary batteries. *J. Energy Storage.* 9: 12–24.
- [23] Shiyao Lu., Tianxiang Zhu., Zhaoyang Li., Yuanhao P., Lei Sh., Shujiang D., Guoxin G., (2018), Ordered mesoporous carbon supported $Ni_3V_2O_8$ composites for lithium-ion batteries with long-term and high-rate performance. *J. Mater. Chem. A.* 6: 7005-7013.
- [24] Ravikumar C. R., Kotteeswaran P., Murugan A., Bheema Raju V., Santosh M. S., Nagaswarupa H. P., Nagabhushana H., Prashantha S. C., Anil Kumar M. R., Gurushantha K., (2017), Electrochemical studies of nano metal oxide reinforced nickel hydroxide materials for energy storage applications. *Mater. Today: Proceed.* 4: 12205-12214.
- [25] Dwyer C. O., Gannon G., McNulty D., Buckley D. N., Thompson D., (2012), Accommodating curvature in a highly ordered functionalized metal oxide nanofiber: Synthesis, characterization, and multiscale modeling of

- layered nanosheets. *Chem. Mater.* 24: 3981-3992.
- [26] Pratapkumar C., Prashantha S. C., Nagabhushana H., Anilkumar M. R., Ravikumar C. R., Nagaswarupa H. P., Jnaneshwara D. M., (2017), White light emitting magnesium aluminate nanophosphor: Near ultra violet excited photoluminescence, photometric characteristics and its UV photocatalytic activity. *J. Alloys Comp.* 728: 1124-1138.
- [27] Shilpa Amulya M. A., Nagaswarupa H. P., Anil Kumar M. R., Ravikumar C. R., Kusuma K. B., (2021), Sonochemical synthesis of $MnFe_2O_4$ nanoparticles and their electrochemical and photocatalytic properties. *J. Phys. Chem. Solids.* 148: 109661-109665.
- [28] British national formulary: BNF 69 (69 ed.), (2015), British Medical Association. p. 34. London, *Royal Pharmaceutical Society*.
- [29] Lakshmana Naik R., Kranthi K., Keerthiga G., Raghuram C., (2012), Effect of pyrolysis temperature on cobalt phthalocyanine supported on carbon nanotubes for oxygen reduction reaction. *J. Appl. Electrochem.* 42: 945–951.
- [30] Ravikumar C. R., Kotteeswaran P., Bheema Raju V., Murugan A., Santosh M. S., Nagaswarupa H. P., Prashantha S. C., Anil Kumar M. R., Shivakumar M. S., (2017), Influence of zinc additive and pH on the electrochemical activities of β -nickel hydroxide materials and its applications in secondary batteries. *J. Energy Storag.* 9: 12–24.
- [31] Naveen Kumar A., Jnaneshwara D. M., Ravikumar C. R., Anil Kumar M. R., Ananda Murthy H. C., Shshi Shekhar T. R., Jahagirdar A. A., (2020), $La_{10}Si_6O_{27} : Tb^{3+}$ nanomaterial; its photocatalytic and electrochemical sensor activities on disperse orange and fast blue dyes. *Sens. Int.* 2: 100076-100080.
- [32] Abebe B., Ravikumar C. R., Amare Zereffa E., Naveen Kumar A., Ananda Murthy H. C., (2021), Photocatalytic and superior ascorbic acid sensor activities of PVA/Zn-Fe-Mn ternary oxide nanocomposite. *Inorg. Chem. Communic.* 123: 108343-108347.
- [33] Avinash B., Ravikumar C. R., Anil Kumar M. R., Santosh M. S., Pratapkumar C., Nagaswarupa H. P., Ananda Murthy H. C., Deshmukh V. V., Bhatt A. S., Jahagirdar A. A., Alam M. W., (2021), NiO bio-composite materials: Photocatalytic, electrochemical and supercapacitor applications. *Appl. Surf. Sci. Adv.* 3: 100049-100054.
- [34] Basavaraju N., Prashantha S. C., Nagabhushana H., Naveen Kumar A., Chandrasekhar M., Shashi Shekhar T. R., Ravikumar C. R., Anil Kumar M. R., Surendra B. S., Nagaswarupa H. P., (2021), Luminescent and thermal properties of novel orange–red emitting $MgNb_2O_6 : Sm^{3+}$ phosphors for displays, photo catalytic and sensor applications. *SN Appl. Sci.* 3: 1-15.
- [35] Shilpa Amulya M. A., Nagaswarupa H. P., Anil Kumar M. R., Ravikumar C. R., Prashantha S. C., Kusuma K. B., (2020), Sonochemical synthesis of $NiFe_2O_4$ nanoparticles: Characterization and their photocatalytic and electrochemical applications. *Appl. Surf. Sci. Adv.* 1: 100023-100028.
- [36] Ranjitha R., Meghana K. N., Dileep Kumar V. G., Bhatt A. S., Jayanna B. K., Ravikumar C. R., Santosh M. S., Madhyastha H., Sakai K., (2021), Rapid photocatalytic degradation of cationic organic dyes using Li-doped Ni/NiO nanocomposites and their electrochemical performance. *New J. Chem., RSC.* 45: 796-809.
- [37] Manjunatha A. S., Pavithra N. S., Shivanna M., Nagaraju G., Ravikumar C. R., (2020), $NaFeS_2$ as a new photocatalytic material for the degradation of industrial dyes. *J. Environ. Chem. Eng.* 8: 104500-104505.
- [38] Kusuma K. B., Manju M., Ravikumar C. R., Nagaswarupa H. P., Shilpa Amulya M. A., Anilkumar M. R., Avinash B., Gurushantha K., Ravikantha N., (2020), Photocatalytic and electrochemical sensor for direct detection of paracetamol comprising γ -aluminium oxide nanoparticles synthesized via sonochemical route. *Sens. Int.* 1:100039-100044.
- [39] Barzinjy A. A., Hamad S. M., Aydin S., Mukhtar H., Ahmed Faiq H. S., (2020), Hussain green and eco-friendly synthesis of Nickel oxide nanoparticles and its photocatalytic activity for methyl orange degradation. *J. Mater. Sci: Mater. Electron.* 31: 11303–11316.
- [40] Ravikumar C. R., Kotteeswaran P., Santosh M. S., Shruthi B., Bheemaraju V., Shivakumar M. S., Nagaswarupa H. P., (2016), Microstructure and electrochemical distinctiveness of [Beta]-nickel hydroxide by means of zinc additive and pH. *Asian J. Chem.* 28: 221-229.
- [41] Inamdar A. I., Kim Y. S., Sohn J. S., Im H., Kim H., Kim D. Y., Kalubarme R. S., Park C., (2011), Supercapacitive characteristics of electrodeposited polyaniline Thin films grown on Indium-doped Tin-oxide substrates. *J. Korean Phys. Soc.* 59: 145-149.
- [42] Ankit T., Manish C. J., Kushagra A., Bhuvaneshwari B., Raju K G., (2019), Three-dimensional Nickel Vanadium layered double hydroxide nanostructures grown carbon cloth for high-performance flexible supercapacitor applications. *Nanosci. Adv.* 1: 2400-2407.